Li *et al. Chin. J. Mech. Eng.* (2020) 33:33
https://doi.org/10.1186/s10033-020-00448-0

Chinese Journal of Mechanical Engineering

ORIGINAL ARTICLE Open Access

Effect of Trace Addition of Ceramic on Microstructure Development and Mechanical Properties of Selective Laser Melted AlSi10Mg Alloy

Yuxin Li, Dongdong Gu*, Han Zhang and Lixia Xi

Abstract

Selective laser melting (SLM) is an emerging additive manufacturing technology for fabricating aluminum alloys and aluminum matrix composites. Nevertheless, it remains unclear how to improve the properties of laser manufactured aluminum alloy by adding ceramic reinforcing particles. Here the effect of trace addition of TiB_2 ceramic (1% weight fraction) on microstructural and mechanical properties of SLM-produced AlSi10Mg composite parts was investigated. The densification level increased with increasing laser power and decreasing scan speed. A near fully dense composite part (99.37%) with smooth surface morphology and elevated inter-layer bonding was successfully obtained. A decrease of lattice plane distance was identified by X-ray diffraction with the laser scan speed decreased, which implied that the crystal lattices were distorted due to the dissolution of Si and TiB_2 particles. A homogeneous composite microstructure with the distribution of surface-smoothened TiB_2 particles was present, and a small amount of Si particles precipitated at the interface between reinforcing particles and matrix. In contrast to the AlSi10Mg alloy, the composites showed a stabilized microhardness distribution. A higher ultimate tensile strength of 380.0 MPa, yield strength of 250.4 MPa and elongation of 3.43% were obtained even with a trace amount of ceramic addition. The improvement of tensile properties can be attributed to multiple mechanisms including solid solution strengthening, load-bearing strengthening and dispersion strengthening. This research provides a theoretical basis for ceramic reinforced aluminum matrix composites by additive manufacturing.

Keywords: Selective laser melting, TiB_2, Aluminum matrix composites, Mechanical properties, Strengthening mechanism

1 Introduction

Aluminum alloys are known for their lightweight, low thermal expansion, high specific strength and high toughness widely used in the industries of aerospace and automobile. In recent years, there has been an increasing demand for high performance and lightweight metals among various industries. However, aluminum alloys are confronted with great difficulties for their limited applicability caused by poor wear resistance and low hardness [1, 2]. In order to address these problems, aluminum matrix composites (AMCs) reinforced with ceramic particles have been greatly developed, thus better adapt to the current and future applications. It is well known that several crucial factors affect the mechanical performances of AMCs, including the matrix microstructure, uniformity of reinforcement and interfacial bonding strength of reinforcement/matrix [3, 4]. In conventional processes, some common process problems usually arise for producing AMCs, including the agglomeration of reinforcements, interfacial defects and poor adhesion at

*Correspondence: dongdonggu@nuaa.edu.cn
College of Materials Science and Technology, Nanjing University of Aeronautics and Astronautics, Nanjing 211106, China

the interface. Indeed, manufacturing complex-shaped components from AMCs is also severely limited through conventional methods [5]. To this end, it is particularly necessary to develop a new processing method for high performance AMCs with complex shapes [6].

Additive Manufacturing (AM), as an emerging advanced layer-by-layer manufacturing technology, is becoming increasingly attractive for industrial applications. Selective laser melting (SLM) is a newly developed powder bed technique allowing for the rapid fabrication of three-dimensional shapes with complex geometries. It uses a moving laser beam that selectively fuses and consolidates thin layers of a loose powder based on computer-aided design (CAD) models [7–10]. It has significant advantages in saving manufacturing time, production cost and reducing personnel error rate [11, 12]. Compared with steels, nickel alloys and titanium alloys [13–15], previous studies have shown that SLM processing of aluminum alloys is much challenging owing to their low absorptivity (only 9%) to the laser beam and the high heat conductivity (237 W/(m·K)) [16]. Up till now, some studies have been carried out to testify to the possibility of AMCs reinforced with ceramics by SLM. For example, Gu et al. fabricated nearly fully dense SLM-processed nanocomposites by adding 5%TiC into AlSi10Mg, wherein obtained high tensile strength of 486 MPa and microhardness of 188 $HV_{0.1}$ [17]. They also investigated in detail the strengthening mechanisms of aluminum matrix composites with different ceramic reinforcing phases, such as SiC [18] and AlN [19] by SLM. The contents of the reinforcing phase were 20% and 5%, respectively. Assorted ceramic reinforcing particles have been successfully applied to AMCs via SLM technology. Likewise, Titanium diboride (TiB_2) is an appealing candidate for its high melting point (3173 K), high modulus (565 GPa), high hardness (2500 HV), and good thermal stability, which could inhibit or lower the degree of adverse reaction between TiB_2 and Al alloys [20–22].

In view of the aforementioned advantages, SLM of TiB_2 reinforced mental matrix composites (MMC) is being pursued actively. Wang et al. [23] fabricated heat treatable 5%TiB_2/Al-3.5Cu-1.5Mg-1Si composites successfully by SLM, and found that higher strength was achieved after the addition of TiB_2 and heat treatment. Xi et al. [24] prepared near-fully dense 2%TiB_2/Al-12Si composites by SLM. The results showed that improved microhardness (142 ± 6.0 $HV_{0.05}$) and yield strength (247 ± 4.0 MPa) compared to the corresponding HP one. The TiB_2/316L nanocomposites were much studied by Almangour et al. [25, 26]. The influence of nanoscale reinforcement on densification, microstructure and strengthening mechanisms were systematically presented, where TiB_2 was added at 5% or above. Due to the good weldability and well corrosion resistance of AlSi10Mg, it has been widely used in additive manufacturing. However, limited work has been concentrated on TiB_2 reinforcing AlSi10Mg samples by SLM. Li et al. [27] produced fully dense and crack-free samples using SLM with an in-situ nano-TiB_2 decorated AlSi10Mg composite (NTD-Al) powder, where the amount of TiB_2 was as high as 11.6%. Wu et al. [28] analysed the effect of integrated TiB_2 nanoparticles on the anisotropy of the AlSi10Mg component. It is noteworthy that the addition amount of the ceramic reinforcing phase is usually large, and nanoscale ceramic particles have been widely used in previous studies. However, nanoscale reinforcement tends to agglomerate due to the large van der Waals attractive force, therefore high capital investment and time are extremely required. To further expand the knowledge of ceramic reinforced aluminum matrix composites prepared by SLM, the influence of the introduction of a trace amount of ceramics on the aluminum alloy properties needs to be explored. To the best of the authors' knowledge, the effect and mechanism of trace addition of micron ceramic particles reinforced aluminum alloy using SLM have not been clearly studied.

In this study, we turned attention to the selective laser melted 1%micro-TiB_2/AlSi10Mg composite. The influence of processing parameters on densification behavior, surface morphology and interlayer combination is elucidated. Based on the optimal processing parameters, we analyzed the morphology, distribution state and interfacial behavior of TiB_2 particles in the composites using X-ray diffractometer (XRD) and scanning electron microscope (SEM). Simultaneously, their connection with the mechanical properties was established. Several strengthening mechanisms were proposed. These findings would be meritorious references for fabricating TiB_2/AlSi10Mg parts with excellent properties.

2 Materials and Methods

2.1 Powder Preparation

Spherical gas-atomized AlSi10Mg powder (99.8% purity) ranging from 20 μm to 63 μm and TiB_2 powder (99.9% purity) with a size of 3–5 μm (Figure 1a) were served as raw materials. The composite powder components consisting of 1.0 wt.% TiB_2, which were prepared by high energy ball milling in a Pulverisette 6 planetary monomill (Fritsch GmbH, Germany) at a rotation speed of 200 r/min for 4 h. After ball milling, TiB_2 particles were homogenously dispersed around the surfaces of the AlSi10Mg particles, as shown in Figure 1b. At the same time, it can be seen that the ceramic particles have been fragmented to a certain extent.

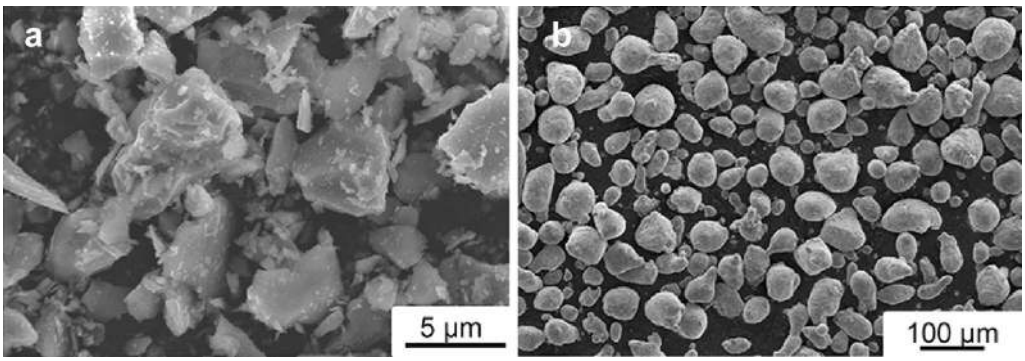

Figure 1 Morphologies of the powder materials: **a** Initial powder of the TiB_2 material; **b** the mixed 1 wt% micro-TiB_2 reinforced AlSi10Mg alloy powder after ball milling

2.2 SLM Process

The as-used device in this study is SLM-150 developed by Nanjing University of Aeronautics and Astronautics (NUAA). The SLM system consists of an IPG Photonics Yitterbium YLR-500-WC fiber laser with a maximal laser power of 500 W and a laser spot diameter of 70 μm, an inert Ar gas protection system, an automatic powder layering system and a computer control system. Initially, an aluminum substrate was set on the building platform and leveled. The building chamber was sealed and Ar gas was pumped into it. Then, the TiB_2/AlSi10Mg composite powders were uniformly spread on the substrate using the automatic powder spreading system until a layer thickness of 50 μm was obtained. The process was repeated until the cubic samples were constructed with a dimension of 10 mm × 10 mm × 8 mm (Figure 2a). An "island scanning strategy" was applied to fabricate specimens, and the orientation of the laser was changed by 37° between successive layers (Figure 2b). The adoption of the island deposition strategy aims to balance the residual stresses in the build [29]. Based on previous experiments, a series of SLM experiments using a wide range of processing parameters, i.e., laser powers of 300–400 W and scan speeds of 2000–3200 mm/s, were performed to testify for the SLM process ability.

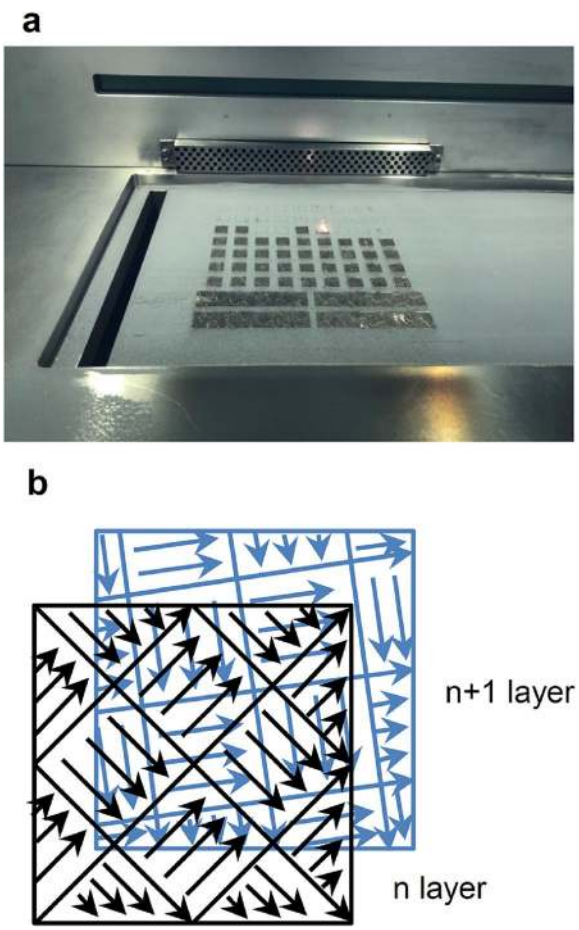

Figure 2 **a** Laser manufacturing process; **b** schematic presentation of laser scanning strategy (checker board with a rotation angle of 37° in successive layers)

2.3 Characterization of Microstructures and Chemical Compositions

The densities of the SLM-processed specimens were measured using the Archimedes principle. Metallographic samples were prepared as per the standard procedures and then etched with Keller's reagent (HF (1.0 mL), HCl (1.5 mL), HNO_3 (2.5 mL), and distilled water (95 mL)) for 30 s. The surface morphology and microstructure were characterized using an optical microscope (OM) and an S-4800 field emission scanning electron microscope (FE-SEM, Hitachi, Tokyo, Japan) at a voltage of 5.0 kV. The chemical compositions were determined by an EDAX energy dispersive X-ray spectroscope

(EDX) (EDAX, Inc., Mahwah, NJ), using a super-ultrathin window sapphire detector. The phases of the specimens were identified through a Bruker D8 Advance X-ray diffractometer (XRD) (Bruker AXS GmbH, Karlsruhe, Germany) with Cu Kα radiation at 40 kV and 40 mA, and the continuous scan mode was used with a scan rate of 4°/min.

2.4 Mechanical Properties

The Vickers hardness was measured using an HXS-1000AY microhardness tester (AMETEK, Shanghai, China) at a load of 0.2 kg and a dwell time of 15 s. Tensile tests using the machine (MTS E45.105) with 0.2 mm/s test speed were performed in accordance with GB/T 228.1-2010 standard at room temperature. Ultimate tensile strength, yield strength and elongation of TiB_2/AlSi10Mg composite and AlSi10Mg alloy samples were achieved. Fractographs of specimens were analyzed by SEM.

3 Results and Discussion

3.1 Densification Behavior and Metallurgical Defect Analysis

Figure 3 shows the variation in the densification behavior of the SLM produced TiB_2/AlSi10Mg composites according to different processing parameters. It is obvious that higher relative densities were obtained under laser power (P) of 400 W. With different laser scan speeds (v), the relative densities also exhibited distinct variations. At a high v of 3200 mm/s, a sample with a relative density of 95.9% was obtained. As the v decreased to 2800 mm/s and 2400 mm/s, relative densities were 97.4% and 98.6%, respectively. Near fully dense part with a relative density of 99.4% was obtained at the lowest v of 2000 mm/s. Thus the relative densities were increased as the v decreased under the same P. As the P decreased, the relative densities of the samples decreased accordingly. When the P decreased to 300 W, the relative densities decreased sharply as the v increased, implying a high sensitivity to scan speed.

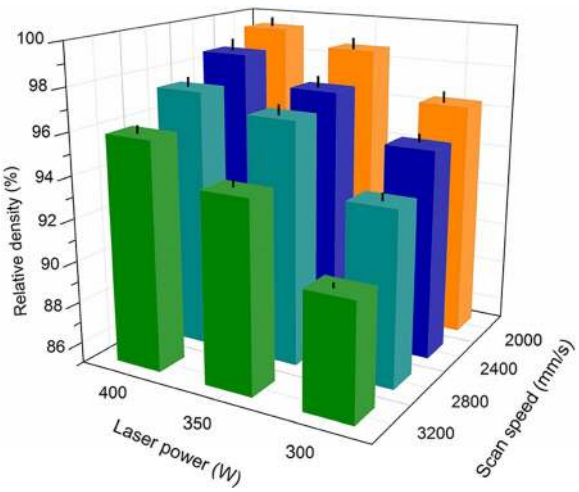

Figure 3 Relative densities of SLM-processed TiB_2/AlSi10Mg composite parts with different process parameters

The typical surface morphologies of the SLM-processed TiB_2/AlSi10Mg parts using various laser scan speeds at a laser power of 400 W are displayed in Figure 4. At a relatively high v of 3200 mm/s, an obvious uneven surface containing a large number of irregular-shaped balls and pores was generated. As the v decreased, the balling effect was still present but the pores were reduced clearly, leading to the surface quality improved. When the v reached the minimum value of 2000 mm/s, a relatively smooth surface was obtained with the highest relative density.

The densification behavior is intrinsically associated with the viscosity of high temperature metal melt, wettability and liquid-solid fluid characteristics [30]. In the SLM molten pools, the relationship between dynamic viscosity μ and temperature T can be expressed as:

$$\mu = \frac{16}{15}\sqrt{\frac{m}{k_B}}\gamma, \tag{1}$$

where m is the atomic mass, k is the Boltzmann constant, and γ is the surface tension of the melt. A low scan speed means a long dwelling time of laser beam and high energy input, and the resultant high T results in a decrease of μ. The low viscosity of the liquid phase can improve the liquidity of the metal melt, which also contributes to the wettability between TiB_2 reinforcements and the Al matrix.

Generally, the balling effect is a typical metallurgical defect in the SLM process, which closely related to the temperature of the liquid phase, wetting ability and Marangoni convection [31, 32]. At a high scan speed, the laser tracks easily show a shrinking trend for reducing the surface tension due to the poor wetting characteristic. Through Arafune and Hirata's results [33], the intensity of Marangoni convection can be estimated by dimensionless Marangoni number (Ma) as follows:

$$M_a = \frac{\Delta\sigma L}{\mu\nu_k}, \tag{2}$$

where $\Delta\sigma$ is the surface tension difference of Marangoni flow, L is the length of the free surface, μ is the dynamic viscosity, and ν_k is the kinematic viscosity. It can be concluded that the convection can be reinforced by the decrease of μ within the pools. With the decrease of scan speed, Marangoni convection is intensified as the

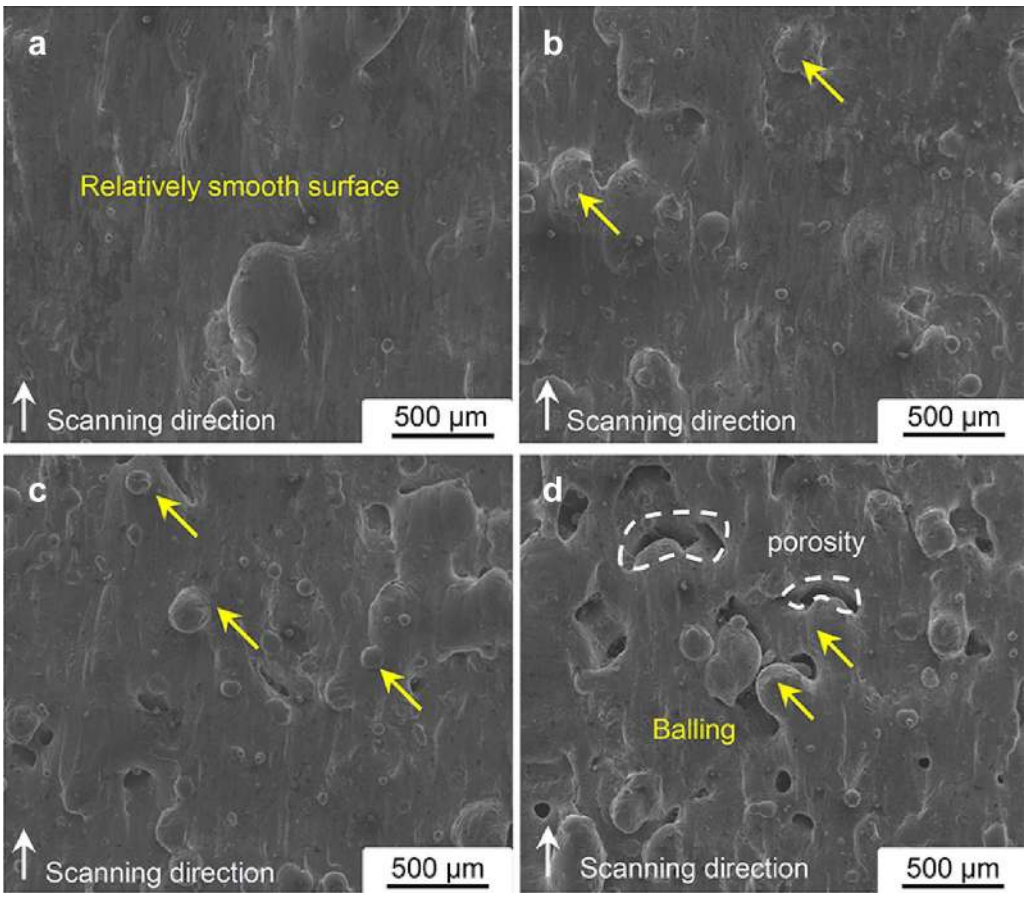

Figure 4 The typical FE-SEM images showing the surface morphologies of SLM-processed TiB_2/AlSi10Mg composite parts fabricated by various scan speeds ($P = 400$ W): **a** $v = 2000$ mm/s; **b** $v = 2400$ mm/s; **c** $v = 2800$ mm/s; **d** $v = 3200$ mm/s

viscosity decreases according to Eq. (2), which improves the spreading ability of the molten pool. Therefore molten tracks present a better continuity without balling phenomenon, owing to the well-wetting characteristic [34].

The different interlayer microstructures with different scan speeds are visible upon etching on cross-sections of SLM-processed TiB_2/AlSi10Mg parts (Figure 5). At a high scan speed of 3200 mm/s (Figure 5d), a significant poor interlayer bonding can be observed including several considerable inter-layer pores, which was in line with the density results. As the scan speed decreased to 2800 mm/s (Figure 5c), some small pores still existed, and cracks can be identified in the molten pool. As the scan speed further decreased to 2400 mm/s (Figure 5b), there were no obvious pores and the cross-section showed a relatively heterogeneous layerwise microstructure, indicating the continuity of scanning trace was poor. When the lowest scan speed of 2000 mm/s was used, the molten pool showed a more coherent inter-layer bonding free of residual pores (Figure 5a). The molten pools had a clear configuration, showing a stable solidification process during SLM. The different solidification behaviors are believed to be controlled by the laser energy input and fluid flow conditions. Higher viscosity and surface tension could block the flowability of the melt and reduce the overall rheological performance of the composite melt, thus make it difficult for the liquid phase to expand sufficiently. Simultaneously, balling hinders the spread of the new layer powder on the previous layer, resulting in the formation of inter-layer pores.

3.2 XRD Analysis

Typical XRD characterization corresponding to the α-Al phase of SLM-processed TiB_2/AlSi10Mg parts at different processing parameters is depicted in Figure 6. It is obviously that the 2θ locations of the diffraction peaks for α-Al significantly changed as the variation of applied SLM parameters. Generally, the standard diffraction peaks for the α-Al phase are located at $2\theta = 38.4°$ and $2\theta = 44.7°$ (JCPDS Card No. 04-0787). The corresponding quantitative parameters for composites obtained from

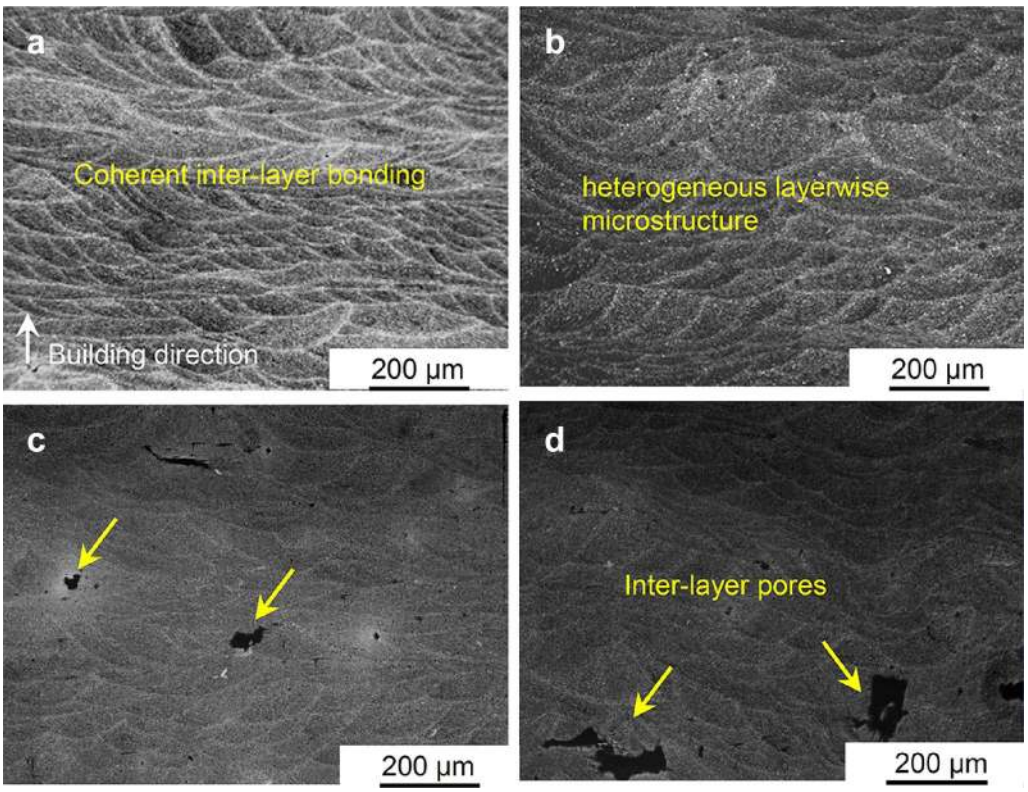

Figure 5 Morphologies of the molten pool on cross sections of SLM-processed TiB_2/AlSi10Mg composite samples at different parameters ($P = 400$ W): **a** $v = 2000$ mm/s; **b** $v = 2400$ mm/s; **c** $v = 2800$ mm/s; **d** $v = 3200$ mm/s

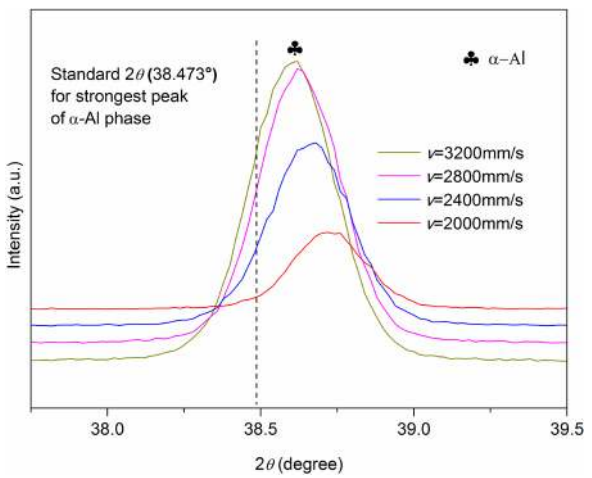

Figure 6 XRD spectra in the vicinity of the strongest diffraction peak at different scan speeds, showing the changes of the α-Al diffraction peak

XRD analysis are listed in Table 1. The specific 2θ locations, intensities and FWHM (Full Width at Half Maximum) of α-Al peaks show obvious changes on account of the addition of TiB_2 and the variation of SLM processing parameters. With the decrease of scan speed, the location of α-Al diffraction peaks shifted to higher 2θ angles. Based on Bragg's law for XRD analysis [35]:

$$2d \sin\theta = n\lambda \quad (n = 1, 2, 3\ldots), \tag{3}$$

the observed increase of 2θ revealed that a decrease in lattice plane distance, implying the crystal lattices were distorted, which was responsible for a small amount of Si and partial micro-TiB_2 particles were dissolved and supersaturated in the Al matrix. The atomic radius of Al, Si, Ti and B are 0.1431 nm, 0.1172 nm, 0.1453 nm and 0.0950 nm, respectively. The replacement solid solution usually generates in α-Al matrix [36], resulting in lattice distortion. With the scan speed decreases, the laser-induced non-equilibrium metallurgical process is reinforced which could dissolve more Si atoms [37]. It is clearly that the atomic radius of Si is smaller than Al, causing the decrease of the lattice plane distance. Table 1 showed the value of FWHM decreased as the v increased. According to Scherrer's formula [38], the increase of FWHM reveals the crystalline size reduction of the composite. The high scan speed leads to the rapid cooling rate, thus the grain growth is prevented, which is sensitive to the SLM processing parameters.

Table 1 Variation of 2θ locations and intensities of the α-Al diffraction peaks in SLM-processed composites with different scan speeds

Sample	2θ (°)	Intensity (cps)	FWHM (rad)	2θ (°)	Intensity (cps)	FWHM (rad)
Standard	38.472	–	–	44.738	–	–
$v=2000$ mm/s	38.720	6329.17	0.268	44.981	3104.17	0.294
$v=2400$ mm/s	38.679	15129.2	0.293	44.920	6879.17	0.309
$v=2800$ mm/s	38.620	22679.2	0.286	44.880	11079.2	0.329
$v=3200$ mm/s	38.619	24795.8	0.301	44.880	11533.3	0.328

3.3 Distribution State of the Micro-TiB_2 Reinforcing Particles

The SEM image and corresponding EDX mapping analysis reveal the distribution state of the TiB_2 reinforcing particles at v=2000 mm/s that obtained the highest relative density (Figure 7). Figure 7a shows the homogeneous distribution state of TiB_2 particles. To further elucidate the particles were TiB_2, the corresponding element EDX mappings of the Al, Si, Mg, Ti and B are given in Figure 7b–f, respectively. Obviously, these particles were TiB_2 phase as represented by the concentration of Ti.

In the solidification microstructures generated by traditional casting [39], the majority of TiB_2 particles aggregate easily. However, in this study, the clustered particles were dispersed effectively, which could be contributed to the ball milling procedure and SLM process. For the low scan speed, the enhanced Marangoni convection and flowability of the melt promote the movement of TiB_2 particles, improving their uniform distribution and the wettability between reinforced particles and the matrix. Furthermore, particle pushing and engulfment can not be ignored in particulate-reinforced metal matrix composite systems, which contributes to a relatively uniform distribution of particles [39].

3.4 Morphology Variation and Interfacial Behavior of Micro-TiB_2 Particles

The morphology of TiB_2 particles in SLM-processed composite is illustrated in Figure 8a. Compared to the initial powder (Figure 1a), it could be observed that the TiB_2 particles became more round and smooth after the

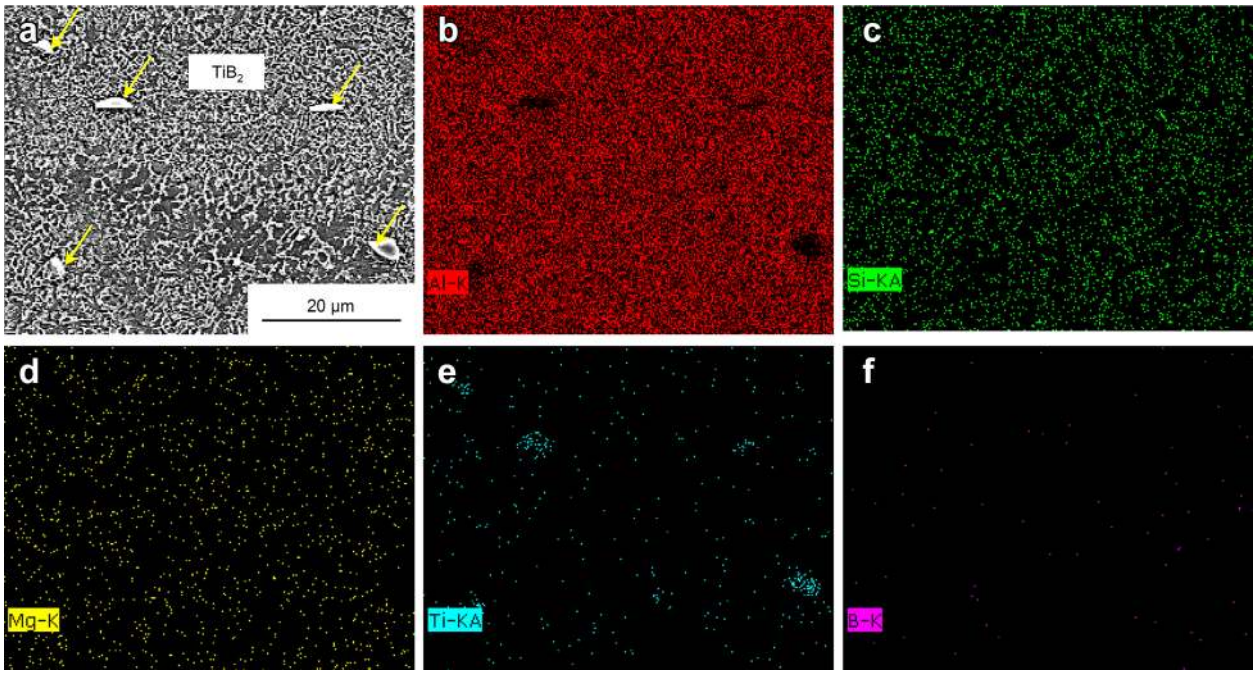

Figure 7 **a** FE-SEM image showing the dispersion morphologies of micro-TiB_2 particles in the matrix at optimized laser processing parameter (P = 400 W and v = 2000 mm/s); **b**–**f** EDX element mappings of (**a**) showing the distribution of Al, Si, Mg, Ti, B, respectively

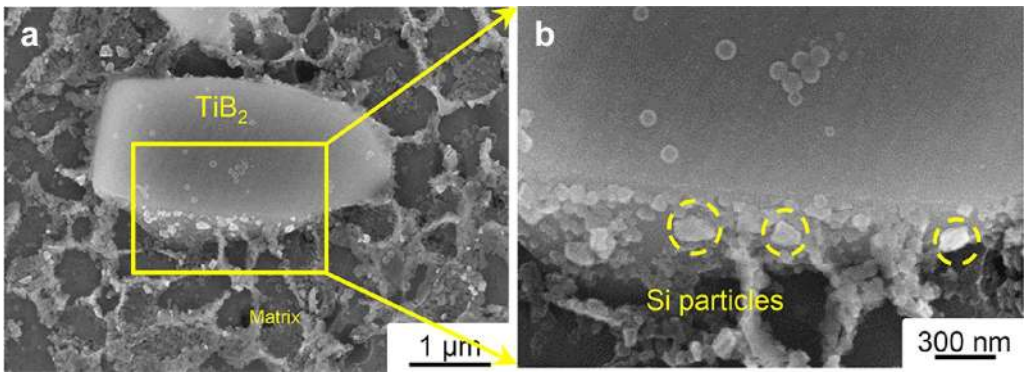

Figure 8 **a** FE-SEM images showing the morphology of the TiB_2 particle after SLM process; **b** high-magnification image showing the interface between TiB_2 particle and matrix, taking from the rectangle in **a**

SLM process, indicating that they are partially melted. No obvious reaction products were observed, implying the melted TiB_2 dissolved into the matrix. This is consistent with the XRD results. Generally, the laser absorption efficiency of ceramics is better than that of metals [18]. Sufficient laser energy input makes the heat concentrate on the TiB_2 easily, causing the melt of TiB_2 particles although they have a high melting point (3225 °C [40]). The sharp edges of the particles tend to concentrate energy, where melt preferentially and generate smooth edges.

It has been reported that TiB_2 particles and α-Al grains tend to form a high-coherency orientation relationship between the two atomic structures to reduce the solid-particle interfacial energy [39]. The smooth TiB_2 particles in uniform dispersion and attendant enhanced wettability between reinforcement and aluminum matrix contribute to the formation of coherent interfaces. There were no palpable voids or reaction products can be seen near the interface, indicating that the interface between the TiB_2 particles and the matrix was well integrated. Further, a small amount of spherical particles could be seen precipitating at the interface (see the rectangle in Figure 8a). Figure 8b shows a high-magnification SEM image from the local region of Figure 8a, where coarse particles at the interface are shown more clearly. For the micro-scale TiB_2, there has not been evidentially reported reacting with the aluminum matrix. However, eutectic Si tends to form a rod- or needle-like coarse microstructure (usually tens to hundreds of microns in size) in conventional casting Al alloy [41]. It is well known that the rapid cooling process can lead to significant extended (non-equilibrium) solid solubility in alloys [42, 43]. Thus the SLM process can dissolve more Si phase compared with the traditional casting technology due to its extremely high cooling rate. With the low scan speed of 2000 mm/s, the cooling rate decreased and the eutectic Si phase has ample time to precipitate from the Al matrix. The TiB_2 particles affect the distribution of Si particles in the matrix. On the one hand, it has been reported that boride particles with spherical morphology would increase the chance of exposing crystallographic plane suitable for precipitation [44]. On the other hand, the presence of TiB_2 particles could cause chemical inhomogeneity, and these particles can act as good heterogeneous nucleation sites for the formation of Si particles. Therefore, it can be concluded that these nano-particles precipitated at the interface are probably Si particles.

3.5 Mechanical Properties

Figure 9 illustrates the microhardness and its distribution measured along the building direction of SLM-processed AlSi10Mg alloy and TiB_2/AlSi10Mg composite parts. Compared with the microhardness of AlSi10Mg alloy, the average microhardness of the composite (120.0 HV) was slightly higher than that of the alloy (117.5 HV). Certainly, compared with cast AlSi10Mg (95 ~ 105 HV) [45], the microhardness have been both greatly improved. This is attributed to the large distribution of the Si phase in the Al matrix due to the rapid solidification and cooling rate of SLM. Furthermore, the microhardness of the AlSi10Mg part showed a relatively large fluctuation varied from 110.2 HV to 124.4 HV. The values also increased as it was closer to the bottom of the sample. The closer it is to the bottom of the sample, the greater the cooling rate and temperature gradient of the melt will be, causing the larger residual stress, which increases the microhardness. The heat accumulation near the top surface could result in stress release, leading to the reduction of microhardness [45]. The composite part showed a reduced fluctuation of the microhardness values.

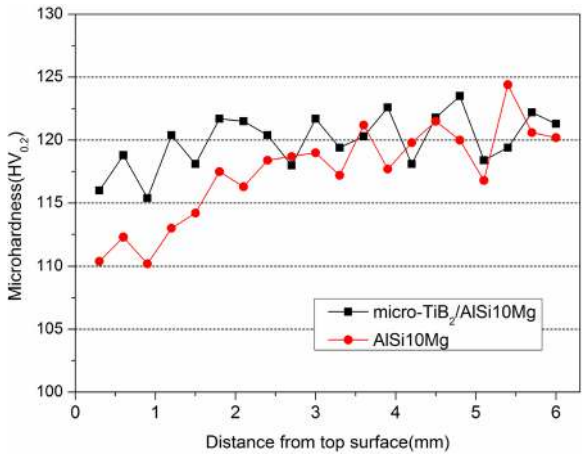

Figure 9 Microhardness distributions of SLM-processed unreinforced AlSi10Mg and micro-TiB_2/AlSi10Mg composite parts along the building direction

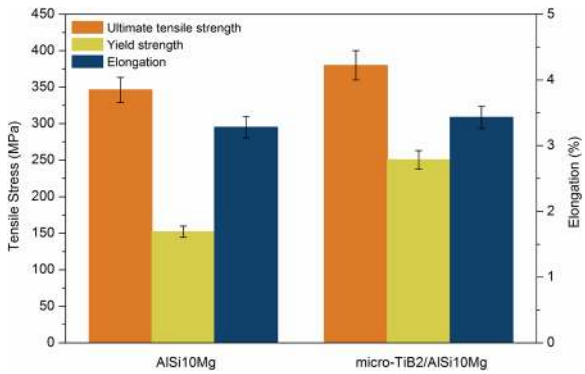

Figure 10 The tensile properties of the unreinforced SLM-processed AlSi10Mg alloy and TiB_2/AlSi10Mg samples including ultimate tensile strength, yield strength and elongation

This can be attributed that the uniformly dispersed TiB_2 particles relieve the stress release and effectively restrain the deformation of the matrix during indentation, hence stabilize and elevate the microhardness value.

The mechanical properties of the TiB_2/AlSi10Mg composite and AlSi10Mg alloy fabricated by SLM were investigated by room temperature tensile tests and the results are provided in Figure 10. The ultimate tensile strength (UTS), yield strength (YS) and elongation of the composite were 380.0 ± 10 MPa, 250.4 ± 6 MPa and 3.43 ± 0.2%, respectively, increased by 9.73%, 64.4% and 4.57% compared to the SLM-processed AlSi10Mg alloy (346.3 ± 8 MPa, 152.3 ± 4 MPa and 3.28 ± 0.15%) under the same processing parameters. It can be seen that both strength and toughness were improved. Figure 11 illustrates the morphologies of the fracture surfaces for the AlSi10Mg part and the TiB_2/AlSi10Mg composite part. Some spherical pores on the fracture surface of the AlSi0Mg could be observed clearly (Figure 11a), these porosities maybe the origin of crack initiation and lead to the poor mechanical properties [46]. The fracture surface of the composite shows a flat fracture surface free of macro-pores (Figure 11c). Moreover, the fracture surfaces at high-magnification were both apparently covered with dimples, indicating their plastic fracture characteristics (Figure 11b and d). Obviously, the dimples of TiB_2/AlSi10Mg composite were finer and more uniform than AlSi10Mg alloy, revealing its enhanced plasticity and excellent ability to absorb the energy of the fracture.

It is known that the distribution of the reinforcing particles in the matrix and the degree of bonding between the matrix and reinforcement are the key factors for composites' mechanical properties [41]. It has been proved that TiB_2 particles dispersed uniformly and a strong interfacial bonding was generated (Sections 3.3 and 3.4), which is beneficial for the coordinate deformation between the strengthening particles and the matrix. The smooth edge without a sharp angle of TiB_2 could release the stress concentration and restrain the cracks under external loads. Based on our analysis above, the increment in tensile properties of SLM processed TiB_2/AlSi10Mg composite is attributed to these three reasons: (I) The dissolved Si and TiB_2 phases result in lattice distortion of Al, forming local stress fields which could interact with dislocations and restrain their motion. Hence, the tensile strength is improved. (II) The uniformly dispersed micro-TiB_2 particles effectively inhibit the slipping of dislocation during deformation via the Orowan mechanism. (III) The strong interfacial bonding between the micro-particles and the matrix facilitates the transfer of the load from the aluminum matrix to TiB_2 particles [41, 45, 47–49]. The strengthening effect caused by load transfer on yield strength can be specifically expressed by the shear lag model modified by Nardone and Prewo [50]:

$$\sigma_c = \sigma_m \left[\frac{V_p(s+4)}{4} + V_m \right], \tag{4}$$

where σ_c and σ_m are the yield strengths of composite and the alloy (~152.3 MPa), respectively. V_p and V_m are the volume fraction of the reinforcing phase and matrix (~1 vol% and ~99 vol%), s is the aspect ratio of TiB_2 (~2.5). As such, the calculate σ_c is 153.3 MPa. It contributes more to the improvement of yield strength. Orowan strengthening via dispersed TiB_2 particles in the matrix is expressed by the equation [50, 51]:

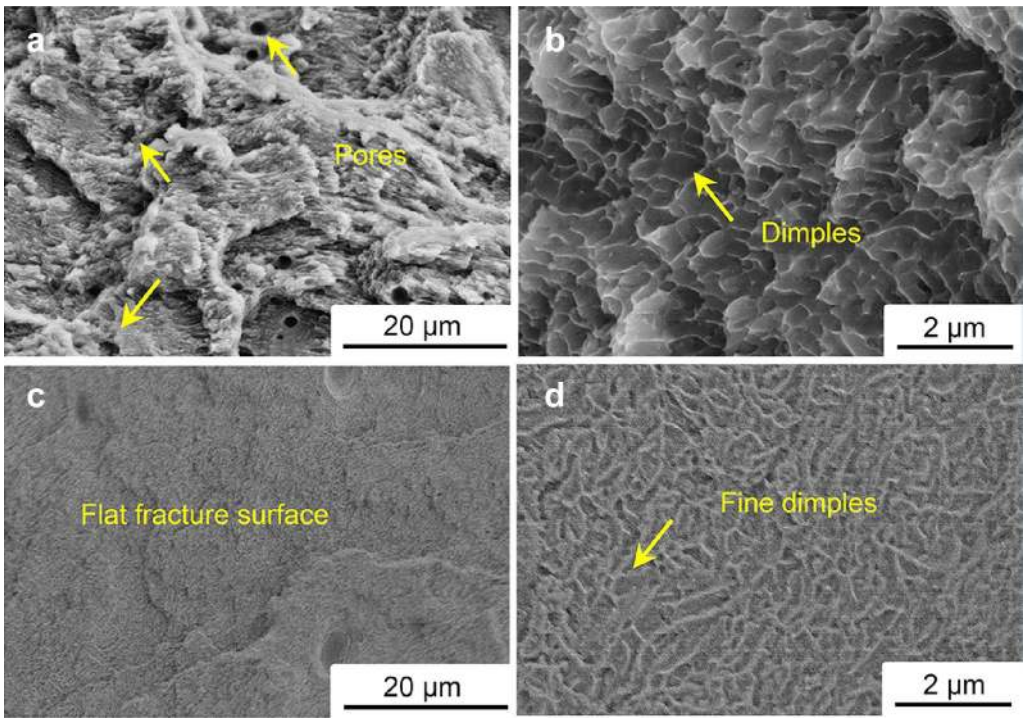

Figure 11 Typical FE-SEM fracture morphologies taken from the tensile fracture surface of samples at room temperature tensile test: low magnification **a** AlSi10Mg and **c** TiB_2 /AlSi10Mg; high magnification **b** AlSi10Mg and **d** TiB_2 /AlSi10Mg

$$\Delta\sigma_{or} = 2Gb/\lambda, \tag{5}$$

$$\lambda = 0.6d_p\left(\frac{2\pi}{V_P}\right)^{1/2}, \tag{6}$$

where G is the shear modulus of the matrix (2.59×10^4 MPa), b is the Burger's vector (0.286 nm), d_p denotes the average particle diameter (4 μm). The estimated strength from the Orowan strengthening is just 0.246 MPa. It is worth noting that this contribution is negligible compared with load transfer strengthening. Solid solution strengthening has been proved to exist in both alloy and composites [27, 45]. In this study, the solid solution strengthening is weakened due to the precipitation of the Si phase, and it is inappreciable compared with alloy for composite. Therefore, load-bearing is the major strengthening mechanism for micro-TiB_2/AlSi10Mg composite.

4 Case Study

Aluminum alloy has become a widely used metal material in aerospace parts. Figure 12 shows the tubing parts for aero engines using TiB_2/AlSi10Mg powder by SLM. The optimal processing parameter ($P=400$ W, $v=2000$ mm/s) was adopted. Figure 12a shows the 3D model in Materialise Magics software. The top view of the model is shown in Figure 12b. The full picture and details of the tubing are fully displayed. For details, the inner diameter of the tubing cylinder is 35 mm. The high quality parts were successfully fabricated by SLM (Figure 12d). Obviously, network support structure was used in the fabrication process. These supports ensure the successful manufacture of complex parts, especially those with overhanging structures, and provide a way to dissipate heat during solidification and reduce thermal deformation. The study shows that SLM technology has a broad application prospect in processing aluminum matrix composites with tailored microstructures and performances.

5 Conclusions

In this study, SLM was utilized to process TiB_2/AlSi10Mg composite parts with different parameters. The effects of TiB_2 micro-addition on the microstructure and mechanical properties of SLM-produced AlSi10Mg composite parts have been investigated in detail. The main conclusions of the study are the following:

(1) The densification behavior was controlled by the scan speed and laser power. A combination of high laser power ($P=400$ W) and low scan speed ($v=2000$ mm/s) resulted in a high relative density which could be up to 99.37%. Relatively smooth surface morphology was generated accordingly owing to sufficient energy

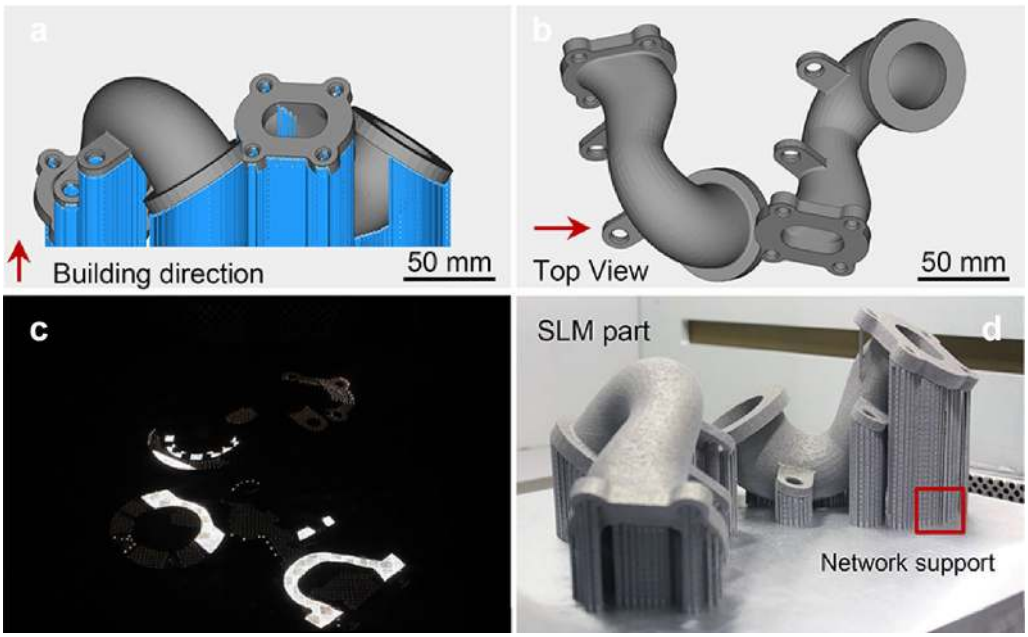

Figure 12 **a** The model in Materialise Magics; **b** top view of the model; **c** the photo of SLM processing; **d** complex shaped Al-based components fabricated by SLM

input. With the decrease of scan speed, the balling effect was inhibited and the molten pool became coherent free of residual pores.

(2) The XRD results revealed the lattice plane distance decreased with scan speed decreased, implying the lattice distortion was generated after the SLM process. The SEM results showed that a uniform dispersion of TiB_2 particles with smooth and round edges was obtained in the composite part. There was a coherence and strong interface bonding between the TiB_2 particle and aluminum matrix, where some small Si particles distributed at the interface.

(3) Compared to AlSi10Mg alloy, the trace addition of TiB_2 stabilized the microhardness distribution along the building direction and increased the average value slightly. Simultaneously, the tensile properties were remarkably enhanced. Higher ultimate tensile strength, yield strength and elongation (380.0 MPa, 250.4 MPa and 3.42%) were obtained for composite. The strengthening mechanisms can be summarized in three aspects: solid solution strengthening, load-bearing strengthening and dispersion strengthening. Load-bearing is the major strengthening mechanism for the composite.

(4) Based on the optimal processing parameters, the high-quality Al-based complex aircraft parts were successfully fabricated by SLM (Additional file 1).

Supplementary information

Supplementary information accompanies this paper at https://doi.org/10.1186/s10033-020-00448-0.

Additional file 1. Laboratory introduction.

Acknowledgements
Not applicable

Authors' Contributions
DG conceived the idea and was in charge of the whole study; YL, HZ and DG wrote the manuscript; YL, DG and LX were in charge of sampling and laboratory analyses. All authors read and approved the final manuscript.

Authors' Information
Yuxin Li, born in 1996, is currently a master candidate at *College of Materials Science and Technology, Nanjing University of Aeronautics and Astronautics, China.*
Dongdong Gu, born in 1980, is currently a professor and a PhD candidate supervisor at *College of Materials Science and Technology, Nanjing University of Aeronautics and Astronautics, China*. His research interests include laser additive manufacturing of high-performance/multi-function metallic components.
Han Zhang, born in 1995, is currently a PhD candidate at *College of Materials Science and Technology, Nanjing University of Aeronautics and Astronautics, China.*
Lixia Xi, born in 1987, is currently a lecturer and a master candidate supervisor at *College of Materials Science and Technology, Nanjing University of Aeronautics and Astronautics, China.*

Funding
Supported by National Key Research and Development Program "Additive Manufacturing and Laser Manufacturing" of China (Grant Nos.

2016YFB1100101, 2018YFB1106302); National Natural Science Foundation of China (Grant No. 51735005); Jiangsu Provincial Natural Science Foundation for Youth (Grant No. BK20180439); National Natural Science Foundation of China for Creative Research Groups (Grant No. 51921003); The 15th Batch of "Six Talents Peaks" Innovative Talents Team Program (Grant No. TD-GDZB-001); 2017 Excellent Scientific and Technological Innovation Teams of Universities in Jiangsu Province; Nanjing University of Aeronautics and Astronautics Graduate Innovation Base (Laboratory) Open Fund Project (Grant No. kfjj20190606).

Availability of Data and Materials

The datasets supporting the conclusions of this article are included within the article.

Competing Interests

The authors declare no competing financial interests.

Received: 10 October 2019 Revised: 5 March 2020 Accepted: 31 March 2020
Published online: 15 April 2020

References

[1] S won Lim, T Imai, Y Nishida, et al. High strain rate superplasticity of TiC particulate reinforced magnesium alloy composite by vortex method. *Scripta Metallurgica et Materiala*, 1995, 32(11): 1713–1717.
[2] M O Shabani, A Mazahery. Computational modeling of cast aluminum 2024 alloy matrix composites: Adapting the classical algorithms for optimal results in finding multiple optima. *Powder Technology*, 2013, 249: 77–81.
[3] M Montoya-Dávila, M I Pech-Canul, M A Pech-Canul. Effect of SiCp multimodal distribution on pitting behavior of Al/SiCp composites prepared by reactive infiltration. *Powder Technology*, 2009, 19(3): 196–202.
[4] F Rikhtegar, S G Shabestari, H Saghafian. The homogenizing of carbon nanotube dispersion in aluminium matrix nanocomposite using flake powder metallurgy and ball milling methods. *Powder Technology*, 2015, 280: 26–34.
[5] B AlMangour, D Grzesiak, J M Yang. In-situ formation of novel TiC-particle-reinforced 316L stainless steel bulk-form composites by selective laser melting. *Journal of Alloys and Compounds*, 2017, 706: 409–418.
[6] S Qin, K Cheng. Special issue on future digital design and manufacturing: Embracing industry 4.0 and beyond. *Chinese Journal of Mechanical Engineering*, 2016, 29(6): 1045–1045.
[7] D Herzog, V Seyda, E Wycisk, et al. Additive manufacturing of metals. *Acta Materialia*, 2016, 117: 371–392.
[8] J P Kruth, G Levy, F Klocke, et al. Consolidation phenomena in laser and powder-bed based layered manufacturing. *CIRP Annals - Manufacturing Technology*, 2007, 56(2): 730–759.
[9] B Zhang, Y Li, Q Bai. Defect formation mechanisms in selective laser melting. *Chinese Journal of Mechanical Engineering*, 2017, 30(3): 515–527.
[10] S F Wen, X T Ji, Y Zhou, et al. Corrosion behavior of the S136 mold steel fabricated by selective laser melting. *Chinese Journal of Mechanical Engineering*, 2018, 31:108, https://doi.org/10.1186/s10033-018-0312-8.
[11] G H Song, S K Jing, F L Zhao, et al. Design optimization of irregular cellular structure for additive manufacturing. *Chinese Journal of Mechanical Engineering*, 2017, 30(5): 1184–1192.
[12] Zhang S, Li Y, Hao L, et al. Metal-ceramic bond mechanism of the Co-Cr alloy denture with original rough surface produced by selective laser melting. *Chinese Journal of Mechanical Engineering*, 2014, 27(1): 69–78.
[13] A Simchi, H Pohl. Direct laser sintering of iron-graphite powder mixture. *Materials Science and Engineering A*, 2004, 383(2): 191–200.
[14] D D Gu, Y C Hagedorn, W Meiners, et al. Nanocrystalline TiC reinforced Ti matrix bulk-form nanocomposites by Selective Laser Melting (SLM): Densification, growth mechanism and wear behavior. *Composites Science and Technology*, 2011, 71(13): 1612–1620.
[15] B Song, S Dong, P Coddet, et al. Microstructure and tensile behavior of hybrid nano-micro SiC reinforced iron matrix composites produced by selective laser melting. *Journal of Alloys and Compounds*, 2013, 579: 415–421.
[16] E O Olakanmi. Selective laser sintering/melting (SLS/SLM) of pure Al, Al-Mg, and Al-Si powders: Effect of processing conditions and powder properties. *Journal of Materials Processing Technology*, 2013, 213(8): 1387–1405.
[17] D D Gu, H Q Wang, D H Dai, et al. Rapid fabrication of Al-based bulk-form nanocomposites with novel reinforcement and enhanced performance by selective laser melting. *Scripta Materialia*, 2015, 96: 25–28.
[18] F Chang, D D Gu, D H Dai, et al. Selective laser melting of in-situ Al4SiC4 + SiC hybrid reinforced Al matrix composites: Influence of starting SiC particle size. *Surface and Coatings Technology*, 2015, 272: 15–24.
[19] D H Dai, D D Gu, M Xia, et al. Melt spreading behavior, microstructure evolution and wear resistance of selective laser melting additive manufactured AlN/AlSi10Mg nanocomposite. *Surface and Coatings Technology*, 2018, 349: 279–288.
[20] P Schumacher, A L Greer, J Worth, et al. New studies of nucleation mechanisms in aluminium alloys: implications for grain refinement practice. *Materials Science and Technology*, 2014, 14(5): 394–404.
[21] L Xi, I Kaban, R Nowak, et al. High-temperature wetting and interfacial interaction between liquid Al and TiB2 ceramic. *Journal of Materials Science*, 2015, 50(7): 2682–2690.
[22] A V Smith, D D L Chung. Titanium diboride particle-reinforced aluminium with high wear resistance. *Journal of Materials Science*, 1996, 31(22): 5961–5973.
[23] P Wang, C Gammer, F Brenne, et al. A heat treatable TiB2/Al-35Cu-15Mg-1Si composite fabricated by selective laser melting: Microstructure, heat treatment and mechanical properties. *Composites Part B: Engineering*, 2018, 147: 162–168.
[24] L X Xi, H Zhang, P Wang, et al. Comparative investigation of microstructure, mechanical properties and strengthening mechanisms of Al-12Si/TiB 2 fabricated by selective laser melting and hot pressing. *Ceramics International*, 2018, 44(15): 17635–17642.
[25] B AlMangour, Y K Kim, D Grzesiak, et al. Novel TiB 2 -reinforced 316L stainless steel nanocomposites with excellent room- and high-temperature yield strength developed by additive manufacturing. *Composites Part B: Engineering*, 2019, 156: 51–63.
[26] B Almangour, D Grzesiak, J M Yang. Rapid fabrication of bulk-form TiB2/316L stainless steel nanocomposites with novel reinforcement architecture and improved performance by selective laser melting. *Journal of Alloys and Compounds*, 2016, 680: 480–493.
[27] X P Li, G Ji, Z Chen, et al. Selective laser melting of nano-TiB2decorated AlSi10Mg alloy with high fracture strength and ductility. *Acta Materialia*, 2017, 129: 183–193.
[28] Y K Xiao, Z Y Bian, Y Wu, et al. Effect of nano-TiB_2 particles on the anisotropy in an AlSi10Mg alloy processed by selective laser melting. *Journal of Alloys and Compounds*, 2019, 798(25): 644–655.
[29] N Read, W Wang, K Essa, et al. Selective laser melting of AlSi10Mg alloy: Process optimisation and mechanical properties development. *Materials and Design*, 2015, 65: 417–424.
[30] C Qiu, C Panwisawas, M Ward, et al. On the role of melt flow into the surface structure and porosity development during selective laser melting. *Acta Materialia*, 2015, 96: 72–79.
[31] N K Tolochko, S E Mozzharov, I A Yadroitsev, et al. Balling processes during selective laser treatment of powders. *Rapid Prototyping Journal*, 2004, 10(2): 78–87.
[32] D Brown, C Li, Z Y Liu, et al. Surface integrity of Inconel 718 by hybrid selective laser melting and milling. *Virtual and Physical Prototyping*, 2018: 2759.
[33] K Arafune, A Hirata. Thermal and solutal marangoni convection in In-Ga-Sb system. *Journal of Crystal Growth*, 1999, 197(4): 811–817.
[34] R Li, J Liu, Y Shi, et al. Balling behavior of stainless steel and nickel powder during selective laser melting process. *International Journal of Advanced Manufacturing Technology*, 2012, 59(9–12): 1025–1035.
[35] D D Gu, Y C Hagedorn, W Meiners, et al. Densification behavior, microstructure evolution, and wear performance of selective laser melting processed commercially pure titanium. *Acta Materialia*, 2012, 60(9): 3849–3860.
[36] B Liu, B Q Li, Z Li. Selective laser remelting of an additive layer manufacturing process on AlSi10Mg. *Results in Physics*, 2019, 12: 982–988.
[37] N Kang, P Coddet, H Liao, et al. Macrosegregation mechanism of primary silicon phase in selective laser melting hypereutectic Al - High Si alloy. *Journal of Alloys and Compounds*, 2016, 662: 259–262.
[38] C Suryanarayana, M G Norton. X-Ray diffraction : a practical approach. *Microscopy and Microanalysis*, 2019: 273.

[39] P L Schaffer, D N Miller, A K Dahle. Crystallography of engulfed and pushed TiB2 particles in aluminium. *Scripta Materialia*, 2007, 57(12): 1129–1132.
[40] F Chen, F Mao, Z Chen, et al. Application of synchrotron radiation X-ray computed tomography to investigate the agglomerating behavior of TiB2 particles in aluminum. *Journal of Alloys and Compounds*, 2015, 622: 831–836.
[41] X P Li, X J Wang, M Saunders, et al. A selective laser melting and solution heat treatment refined Al-12Si alloy with a controllable ultrafine eutectic microstructure and 25% tensile ductility. *Acta Materialia*, 2015, 95: 74–82.
[42] L P Lam, D Q Zhang, Z H Liu, et al. Phase analysis and microstructure characterisation of AlSi10Mg parts produced by Selective Laser Melting, *Virtual and Physical Prototyping*, 2015: 2759.
[43] M Averyanova, P Bertrand, B Verquin. Studying the influence of initial powder characteristics on the properties of final parts manufactured by the selective laser meiting. *Virtual and Physical Prototyping*, 2011: 2759.
[44] P S Mohanty, J E Gruzleskit. Mecahnism of grainrefinement in Aluminium. *Acta Metallurgica et Materialia,* 2012, 43(5): 2001-2012.
[45] L Z Wang, S Wang, X Hong, Pulsed SLM-manufactured AlSi10Mg alloy: Mechanical properties and microstructural effects of designed laser energy densities. *Journal of Manufacturing Processes*, 2018, 35: 492–499.
[46] D K Do, P Li. The effect of laser energy input on the microstructure, physical and mechanical properties of Ti-6Al-4V alloys by selective laser melting. *Virtual and Physical Prototyping*, 2016: 2759.
[47] P Li, Y Li, Y Wu, et al. Distribution of TiB2 particles and its effect on the mechanical properties of A390 alloy. *Materials Science and Engineering A*, 2012, 546: 146–152.
[48] G Liu, G J Zhang, F Jiang, et al. Nanostructured high-strength molybdenum alloys with unprecedented tensile ductility. *Nature Materials*, 2013, 12(4): 344–350.
[49] L Y Chen, J Q Xu, H Choi, et al. Processing and properties of magnesium containing a dense uniform dispersion of nanoparticles. *Nature*, 2015, 528(7583): 539–543.
[50] Z Zhang, D L Chen. Consideration of Orowan strengthening effect in particulate-reinforced metal matrix nanocomposites: A model for predicting their yield strength. *Scripta Materialia*, 2006, 54(7): 1321–1326.
[51] A Sanaty-Zadeh. Comparison between current models for the strength of particulate-reinforced metal matrix nanocomposites with emphasis on consideration of Hall-Petch effect. *Materials Science and Engineering A*, 2012, 531: 112–118.